Characterization of Distributed Birefringence in Optical Fibers

31

Yongkang Dong, Lei Teng, Hongying Zhang, Taofei Jiang, and Dengwang Zhou

Contents

Abstract

Birefringence is the fundamental physical parameter of optical fibers which characterizes their polarization properties, and it can be classified into phase birefringence and group birefringence. Phase birefringence is the difference in effective index between the two orthogonal linear polarization modes of an optical fiber, while the group birefringence is related to group index representing the polarization mode dispersion. In this chapter, we introduce a distributed phase birefringence measurement method based on Brillouin dynamic grating

Y. Dong (✉) · L. Teng · T. Jiang · D. Zhou
National Key Laboratory of Science and Technology on Tunable Laser, Harbin Institute of Technology, Harbin, China
e-mail: aldendong@163.com; aldendong@gmail.com; tengl_hit@163.com; jiangtaofei390@126.com; cishixitie@163.com

H. Zhang
Institute of Photonics and Optical Fiber Technology, Harbin University of Science and Technology, Harbin, China
e-mail: zhy_hit@163.com

G.-D. Peng (ed.), *Handbook of Optical Fibers*,
https://doi.org/10.1007/978-981-10-7087-7_60

(BDG), which creates a new horizon for optical fiber evaluation. When two parallel polarized pump waves, with a frequency offset equal to the fiber Brillouin frequency shift, counter-propagate along the fiber, a BDG can be excited through simulated Brillouin scattering (SBS), and another orthogonally polarized probe wave injected into fiber is used to detect the BDG. When the frequency difference between the probe wave and the co-propagating pump wave meets the phase-matching condition, the maximum reflection on probe wave from the BDG can be obtained. The interaction of the excitation and the probing of a BDG involves four optical waves, and the Brillouin-enhanced four-wave mixing model completely describes this coupling process. In the following sections of this chapter, the theoretical operation principles, numerical simulations, and experimental implementation of distributed phase birefringence measurement with BDG are described; some sensing applications of distributed birefringence measurement with BDG are also given including simultaneous distributed temperature and strain measurement, distributed transverse pressure sensing, and distributed hydrostatic pressure sensing.

Keywords
Birefringence · Polarization-maintaining fiber · Distributed measurement · Stimulated Brillouin scattering · Brillouin dynamic grating

Introduction

This chapter includes an introduction to and review of the principles of distributed phase birefringence measurement in the case of a polarization-maintaining fiber (PMF) based on the Brillouin dynamic grating (BDG). The primary motivations of the technique are introduced, a description provided the operation principles upon which a BDG is generated and detected, and a detailed examination of the particular manner in which the distributed phase birefringence measurement based on the BDG is undertaken. These are followed by a review of selected real sensing applications investigated for particular sensing areas, together with details of a range of experimental systems and data.

The applications of single-mode fibers (SMFs) to coherent optical fiber communication systems and fiber sensor systems require a definite state of polarization along the fiber length (Keiser 2003). It is well known that in a conventional SMF with imperfect circular cross-section geometry and asymmetrical material distribution, the polarization state of the output signal is usually random; the mode coupling and the output polarization state are highly sensitive to external perturbations. PMFs such as shape-induced PMF, with an elliptical core, and stress-induced PMF, e.g., Panda fiber, have a high internal birefringence that exceeds external perturbing birefringence and maintains linear polarization along the fiber (Kaminow 1981; Noda et al. 1986). PMFs are birefringent in principle: as the two polarization states propagate with slightly different velocities, and when a broadband source is used, the spurious cross-state waves lose coherence with the

main primary signal. The mode coupling between the two orthogonal polarization modes is minimized in a PMF, because the difference between their propagation constants is large (Eugene 2002). Among the fundamental parameters characterizing the polarization-maintaining properties of a PMF, birefringence is a critical one.

There are two definitions of birefringence to describe the polarization properties of a high-birefringence fiber: one is the phase birefringence Δn, i.e., the difference in effective refractive indexes n_x and n_y between the two orthogonal linear polarization modes (Eugene 2002):

$$\Delta n\,(\lambda) = n_x\,(\lambda) - n_y\,(\lambda) \tag{1}$$

which is associated with the polarization beat length $L_B(\lambda)$ by

$$L_B\,(\lambda) = \lambda/\Delta n\,(\lambda) \tag{2}$$

and the other is the group birefringence Δn^g

$$\Delta n^g\,(\lambda) = n_x^g\,(\lambda) - n_y^g\,(\lambda) = \Delta n\,(\lambda) - \lambda\frac{\mathrm{d}\Delta n\,(\lambda)}{\mathrm{d}\,(\lambda)}. \tag{3}$$

The group birefringence is closely related to polarization mode dispersion (PMD) $\tau = \Delta n^g(\lambda)/\mathrm{c}$, which limits the fiber transmission system (Wai and Menyak 1996). Here, n_i and $n_i{}^g$ denote the phase and group refractive indexes which are related to the phase velocity and group velocity, respectively, and c is the velocity of light in a vacuum (Eugene 2002). In telecommunications, it is extremely important to limit the impacts of PMD, while in other applications, such as polarimetric optical sensors, a high value of the phase birefringence is required.

The development of the fiber-optic gyroscope has meant that it has become the main application area for PMFs. To solve the problems of polarization-induced signal fading and lack of the polarization rejection, the development of the high-quality PMF is an important step toward a compact and practical device. In a fiber gyro, the polarization conservation maintains most of the power in the primary reciprocal wave, avoiding signal fading.

A cross-polarization coupling point could occur due to the external perturbation, and the main and crossed wave trains lose their overlap. At this point, a phase mismatch exists because of the different velocities, which leads to the statistical decorrelation between both crossed polarizations (Lefevre 2014).

From the above analyses, it can be found that the polarization-maintaining characters of a PMF play a significant role in practical applications, and the measurement of birefringence is very important for characterizing the polarization properties of the PMF, especially in fiber gyro monitoring and evaluation.

The value of the phase birefringence is often expressed by the beat length L_B between the two orthogonal polarization modes. Several methods exist to measure the beat length (Kikuchi and Okoshi 1983; Takada et al. 1985; Szczurowski et al. 2011; Huang and Lin 1985; Sikka et al. 1998), and the classic schemes are based on

spectral interferometry and the method of a lateral point-like force applied on the fiber (Kaczmarek 2012; Hlubina and Ciprian 2007).

In the experimental setup of the periodic lateral force method for measuring the beat length shown in Fig. 1, the monochromatic light output from the laser diode (LD) is coupled into a principal polarization mode. At a certain location, a periodic lateral force $\boldsymbol{F}$ is applied over a very short length of the fiber, which can be regarded as a concentrated (point-like) perturbation. The force generates the polarization cross talk, and a fraction of the light is coupled into the polarization mode which is not excited at the input end of the fiber. The force sweeps along the fiber to cause the interference oscillatory intensity changes when observed through a polarization analyzer (Pol.). The interference signal is recorded by photoelectric detector (PD) and data acquisition device (DAQ). And the beat length is measured through dividing the fiber length by the number of oscillations. And the phase birefringence can be obtained from Eq. 2.

The high-birefringence fiber Sagnac loop operates like a wavelength-division-multiplexing filter (Fang and Claus 1995), which follows from the dependence of the phase difference between the two orthogonal polarization modes propagating in the high-birefringence fiber.

Figure 2 shows the experimental setup of a typical Sagnac-based birefringence measurement system. The output light from the broadband light source (BBS) is separated by a 3 dB coupler into two beams that counter-propagate in the opposite directions, which recombine in the coupler after traveling through the loop. The two orthogonal polarization modes in the PMF create an interference pattern in the coupler, which is dependent on the phase difference. The practical measurement accuracy depends on the measurement accuracy of fiber length and spectral resolution of optical spectrum analyzer (OSA) (Kaczmarek 2012).

The typical Sagnac interference coefficient $T(\lambda)$ approximates well to a periodic function of wavelength, which can be described by the formula (Xu et al. 2016; Kim and Kang 2004; Hlubina and Ciprian 2007; Fang and Claus 1995):

$$T(\lambda) = 1 - \cos(\varphi)/2 \tag{4}$$

where φ is the phase difference between the two polarization modes in a PMF with a length of L, defined by the formula of $\varphi = 2\pi\Delta nL/\lambda$.

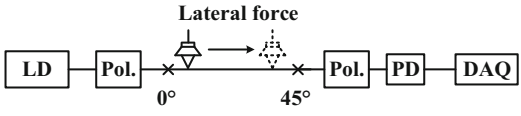

Fig. 1 The typical scheme of the periodic lateral force method for measuring the L_B of the PMF

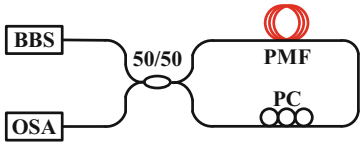

Fig. 2 Experimental setup of birefringence measurement method based on Sagnac

The relationship between the spectrum oscillation and the wavelength changes can be retrieved by calculating the derivative of the phase difference with respect to the wavelength λ, where

$$\frac{\mathrm{d}\varphi}{\mathrm{d}\lambda} = \frac{2\pi L}{\lambda^2}\left[\frac{\mathrm{d}\Delta n}{\mathrm{d}\lambda}\lambda - \Delta n\right] = \frac{2\pi L}{\lambda^2}\left(-\Delta n^{\mathrm{g}}\right). \tag{5}$$

Equation 5 indicates that wavelength scanning of broadband light source yields the group birefringence. And the separation between two adjacent maxima ($\Delta\lambda$) is related to a phase change of 2π and to the group birefringence by

$$\Delta n^{g} = \frac{\lambda^2}{\Delta\lambda L} \tag{6}$$

which shows an approximate solution for the Sagnac-based method measuring the group birefringence.

Although the existing birefringence measurement methods have many advantages, such as simple structures and quick responses, they all belong to the point measurement systems which cannot realize the distributed birefringence measurement. Owing to the nonuniformity of the materials and changes of environmental conditions during the fabrication of the fibers, birefringence variation along the fiber is inevitable. Therefore, it is insufficient to obtain the average birefringence of the PMF for practical applications. Distributed birefringence measurement methods are needed for characterizing the birefringence variation along the fiber (Suzuki et al. 2001).

In 2010, the first truly distributed birefringence measurement of a PMF based on a BDG was reported (Dong et al. 2010a). The results represent the birefringence distribution of two types of widely used PMFs, bow tie fiber and Panda fiber with a length of 8 m and in a spatial resolution of 20 cm. The experimental results confirm that the birefringence features a periodic variation along the fiber. This work was a significant achievement toward the realization of birefringence measurement using BDG. The measurement principles and experimental results of the investigation of the present work, being the primary contents for this chapter, are included in Section III. In addition to the distributed birefringence measurements, the BDG has two unique features when compared with conventional fiber Bragg gratings (FBG): one is that it is a moving grating, which can produce a Brillouin frequency shift (BFS, $\Delta\nu_{\mathrm{B}}$) to the reflected wave with respect to the probe wave, and the other is that a lifetime is associated with it ($\sim$10 ns for silica fiber) for its existence after removing the pump waves (Zhou et al. 2011; Song et al. 2008; Dong et al. 2010b).

To date, the BDG has been generated in a frequency correlation domain (Zou et al. 2009) and time domain (Zhou et al. 2011; Song et al. 2008; Dong et al. 2010a). In the case of the correlation-based technique, a BDG is generated using two synchronized and frequency-modulated continuous pump waves and detected using a separate orthogonally sinusoidal frequency-modulated probe wave (Zou et al. 2009). In the time domain, a BDG can be generated using two

frequency-locked pump waves through stimulated Brillouin scattering (SBS) and can also be generated by a strong pump pulse through spontaneous Brillouin scattering. Moreover, the BDG has been successfully realized in many other platforms besides a PMF (Dong et al. 2009; Song 2012), such as conventional SMF (Song 2011; Dong et al. 2014), dispersion-shifted fibers (Zou and Chen 2013), few-mode fibers (Li and Li 2012), and polarization-maintaining photonic crystal fiber (Dong et al. 2009), and in a photonic chip (Pant et al. 2013), where different acoustic and spatial modes are used in certain materials corresponding to diverse phase relationships.

As well as the basic studies of the theoretical properties of BDG, a wide range of potential applications have been explored, including all-optical information processing (Santagiustina et al. 2013), light storage (Winful 2013), microwave photonics (Sancho et al. 2012), optical delay lines (Chin and Thévenaz 2012), optical spectrum analysis (Dong et al. 2014), and distributed sensing (Dong et al. 2009; Song 2012).

The remaining sections in this chapter are arranged as follows: in the second section, the basic theories of BDG are covered, including the phase-matching condition, the coupled wave equations of the analytical model, and the characteristics of the reflection spectrum; in the third section, distributed birefringence measurement is described in theory and using experiments, and the sensing applications, e.g., distributed temperature, strain, transverse pressure, and hydrostatic pressure measurements, are summarized; and in the last section, the conclusions are presented.

Operation Principle of BDG

The basic operation principles for generating and probing a BDG, the analytical model of the BDG with coupled wave equations of Brillouin-enhanced four-wave mixing (FWM), and some reflection characteristics such as reflectivity and bandwidth are introduced in this section. The contents focus on the discussion of the phase-matching condition and the FWM model explanation for the case of a BDG in PMF.

Theoretical Analysis of BDG

Principle of Generation and Detection of BDG

The Brillouin dynamic grating is similar to a conventional FBG in that they are both examples of local refractive index-modulated grating structures. A brief introduction about the BDG was provided in Section I. In this part, the BDG generation and detection processes in a PMF for the case without depletion are theoretically investigated. The interference of the excitation and probing of the BDG involves four waves interacting with each other through localized density variations of the material, and the resulting reflected wave exhibits a Brillouin frequency difference with respect to the probe wave (Dong et al. 2010b). There are two cases for the

interaction between the probe wave and the BDG: one is that they propagate in the same direction, in which case the reflected wave frequency is down-converted by a fiber BFS through the process of coherent Stokes Brillouin scattering; the other is that they propagate in opposite directions, producing a reflected wave with an up-converted frequency through a fiber BFS in the coherent anti-Stokes Brillouin scattering process.

In the case of coherent Stokes Brillouin scattering, there are two different configurations to perform the birefringence measurement by exchanging the roles of the slow and fast axes, as shown in Fig. 3 (Dong et al. 2010b).

There exists a similar situation for the case of coherent anti-Stokes Brillouin scattering. Therefore, there are a total of four different configurations for generation and detection of a BDG within one PMF by exchanging the options of the slow and fast axes or reversing propagation direction of the probe wave. The following discussions are confined to the case of coherent anti-Stokes Brillouin scattering.

As shown in Fig. 4, a BDG is an optically local refractive index-modulated grating as it is in the case of a FBG. Two counter-propagating pump waves, with a frequency offset of BFS of the PMF, are launched into one axis of the PMF, and SBS occurs when the two pump waves beat together giving rise to density variations associated with acoustic wave propagation within the fiber through the electrostriction effect. The property of the BDG can be detected by monitoring the reflected wave from a probe wave launched into the other axis. The maximum reflection from the BDG can be obtained when the frequency difference between the probe and the co-propagating pump wave satisfies the phase-matching conditions (Song et al. 2008; Dong et al. 2010b).

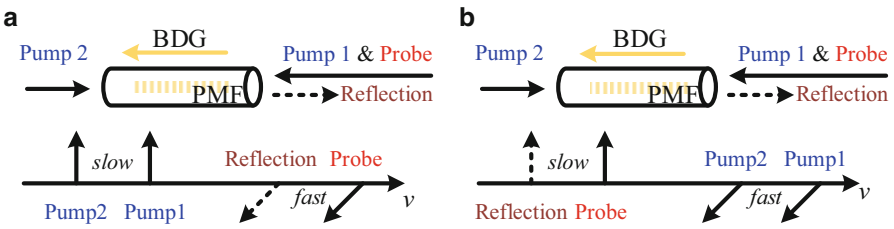

Fig. 3 The schematic representation of two different configurations based on coherent Stokes Brillouin scattering

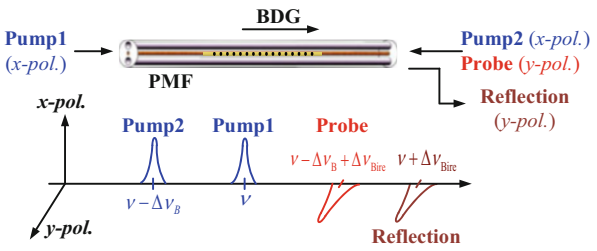

Fig. 4 Schematic diagram of generation and detection of a BDG in PMF

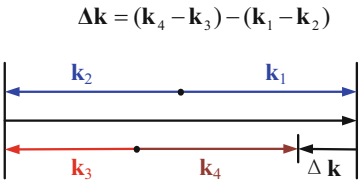

Fig. 5 Wave vector mismatch of the four optical waves

Phase Matching Condition

Due to conservation of momentum during the interaction process of the excitation and the probing of the BDG (Dong et al. 2010a), the four optical waves should meet the criterion of wave vector relationship shown in Fig. 5, where

$$\Delta \mathbf{k} = (\mathbf{k}_4 - \mathbf{k}_3) - (\mathbf{k}_1 - \mathbf{k}_2) \tag{7}$$

and Eq. 7 can also be expressed as

$$\begin{aligned} \frac{2\pi \cdot \Delta \upsilon_{\mathrm{B}}}{V} = & \left(\frac{2\pi \cdot n_y(\upsilon_4)\,\upsilon_4}{\mathrm{c}} + \frac{2\pi \cdot n_y(\upsilon_3)\,\upsilon_3}{\mathrm{c}} \right) \\ & - \left(\frac{2\pi \cdot n_x(\upsilon_2)\,\upsilon_2}{\mathrm{c}} + \frac{2\pi \cdot n_x(\upsilon_1)\,\upsilon_1}{\mathrm{c}} \right) \end{aligned} \tag{8}$$

where V and υ are the acoustic wave velocity and light frequency, respectively, with the former representing the velocity of the BDG.

The phase-matching condition can be derived from the Taylor expansion in Eq. 8 around the refractive indexes of the two axes omitting the higher-order terms, which is

$$\begin{aligned} \frac{n_y(\upsilon_3)\,\upsilon_3}{\mathrm{c}} + \frac{n_y(\upsilon_4)\,\upsilon_4}{\mathrm{c}} = & \frac{n_x(\upsilon_3)\,\upsilon_3}{\mathrm{c}} + (\upsilon_2 - \upsilon_3)\frac{\mathrm{d}\left(n_x(\upsilon_3)\,\upsilon_3\right)}{\mathrm{c}\mathrm{d}\upsilon_3} + \frac{n_x(\upsilon_4)\,\upsilon_4}{\mathrm{c}} \\ & + (\upsilon_2 - \upsilon_3)\frac{\mathrm{d}\left(n_x(\upsilon_4)\,\upsilon_4\right)}{\mathrm{c}\mathrm{d}\upsilon_4} \end{aligned} \tag{9}$$

where $n_x^g(\upsilon_i) = \mathrm{d}\left(n_x(\upsilon_i)\,\upsilon_i\right)/\mathrm{d}\upsilon_i$, where i can be 3 or 4, is denoted as the group refractive index of the x axis, and the Eq. 9 can be simplified as

$$\begin{aligned} (\upsilon_3 - \upsilon_2)\left(n_x^g(\upsilon_3) + n_x^g(\upsilon_4)\right) = & \left(n_x(\upsilon_3) - n_y(\upsilon_3)\right)\upsilon_3 \\ & + \left(n_x(\upsilon_4) - n_y(\upsilon_4)\right)\upsilon_4. \end{aligned} \tag{10}$$

When ignoring the group modal dispersion, the group refractive index satisfies the relation of $n_x^g = n_x^g(\upsilon_3) = n_x^g(\upsilon_4)$. Because that the optical frequency υ (∼hundreds of terahertz) is much larger than the BFS (∼tens of gigahertz) of a fiber, it can be approximately presented that $\upsilon_3 \approx \upsilon_3 + \Delta\upsilon_{\mathrm{B}}$, and then

$$\Delta n\left(v_3\right) = n_x\left(v_3\right) - n_y\left(v_3\right) = n_x\left(v_4\right) - n_y\left(v_4\right). \tag{11}$$

Finally, the phase-matching condition can be obtained as

$$\Delta v_{\text{Bire}} = \Delta n\left(v\right) v / n_x^g \tag{12}$$

where $\Delta v_{\text{Bire}} = (v_3 - v_2)$ is the birefringence-induced frequency shift (BireFS, Δv_{Bire}) and it has a proportional relationship with the phase birefringence $\Delta n(v) = n_x - n_y$.

Coupled Wave Equations of the Brillouin-Enhanced FWM Process

As previously mentioned, the process for the generation and detection of a BDG involves four light waves, two pump waves, a probe waves, and a reflected wave, and the interaction is characterized as Brillouin-enhanced FWM in which the longitudinal acoustic wave couples those four optical waves with different polarization states together (Agrawal 2007; Zhou et al. 2009). Characterization of the BDG spectrum reveals that the shape of the BDG spectrum is similar to that of a weak FBG (Dong et al. 2010b; Erdogan 1997; Song and Yoon 2010).

In the discussions below, the mathematical model for the case of coherent anti-Stokes Brillouin scattering is formulated, with the frequency of the BDG reflection being higher than that of the probe wave. The spatial representation of the four optical waves $\tilde{E}_j$ ($j = 1, 2, 3,$ and 4) and the acoustic wave are illustrated in Fig. 6.

A section of PMF with a horizontal axial coordinate between z = 0 and z = L is considered together with the two orthogonal axes of the x and y directions. Two pump waves (pump 1, $\tilde{E}_1$, and pump 2, $\tilde{E}_2$), with Electric field frequencies of v_1 and v_2, respectively, and a frequency difference equal to the BFS of the fiber of $\Delta v_{\text{B}} = v_1 - v_2$ are injected from opposite directions with the same polarization state (x pol.). An acoustic wave with an amplitude of ρ, frequency of v_{o}, and wave vector of k_5 is then excited by the two pump waves through SBS, which can be expressed in consideration of the medium density modulation, as

$$\tilde{\rho}\left(z,t\right) = \rho_0 + \{\rho\left(z,t\right)\exp\left[i\left(k_5 z - v_{\text{o}} t\right)\right] + c.c.\} \tag{13}$$

where ρ_0 denotes the mean density of the medium.

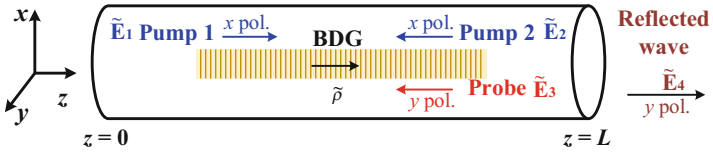

Fig. 6 Scheme of interaction between the optical and acoustic waves in a Brillouin-enhanced FWM process associated with a BDG

The electric fields can be expressed as

$$\tilde{E}_j\,(z,t) = E_j\,(z,t)\exp\left[i\left(k_j z - v_j t\right)\right] + c.c. \tag{14}$$

where $E_j\,(z,\,t)$ ($j = 1,\,2,\,3,$ and 4) represents the amplitude function of position z and time t. And $\boldsymbol{k}_j$ is the wave vector.

The interaction of the four optical waves can be represented as

$$\tilde{E}\,(z,t) = \tilde{E}_1\,(z,t) + \tilde{E}_2\,(z,t) + \tilde{E}_3\,(z,t) + \tilde{E}_4\,(z,t)\,. \tag{15}$$

Considering the electrostriction effect, the equation of medium density modulation can be described as follows:

$$\frac{\partial^2\tilde{\rho}}{\partial t^2} - \Gamma'\nabla^2\frac{\partial\tilde{\rho}}{\partial t} - V^2\nabla^2\tilde{\rho} = \nabla\cdot\mathbf{f} \tag{16}$$

where Γ' and V denote the damping parameter and the velocity of the acoustic wave related to material characteristics, respectively.

Regarded as the source term of Eq. 16, the divergence of the force $\mathbf{f}$ at per unit volume relates to the electrostriction term, by $\mathbf{f} = -\frac{1}{2}\varepsilon_0\gamma_\varepsilon\nabla\left\langle\tilde{E}^2\right\rangle$.

Substituting Eq. 13 into Eq. 16 and considering the slowly varying amplitude approximation, the further material density equation can be obtained as

$$-2i\,v_\mathrm{o}\frac{\delta\rho}{\delta t} - i\,v_\mathrm{o}\Gamma_\mathrm{B}\rho - 2i\,v^2\frac{\delta\rho}{\delta z} = \varepsilon_0\gamma_e k_5\left(E_1E_2^* + E_3^*E_4e^{i\,\Delta k z}\right) \tag{17}$$

where $\Gamma_\mathrm{B} = q^2\Gamma'$ represents the Brillouin linewidth connected with the phonon lifetime $\tau_\mathrm{p} = 1/\Gamma_\mathrm{B}$ and $\Delta k = (k_4 + k_3) - (k_2 + k_1)$ is the phase mismatch of the four optical waves. Due to the orthogonal polarization states of the two pump waves and the probe wave, there are only two driven terms of the practical acoustic field remained in Eq. 16.

The spatial evolution for the interactions can be described using the wave equation

$$\frac{\partial^2\tilde{E}_j}{\partial z^2} - \left(\frac{n}{\mathrm{c}}\right)^2\frac{\partial^2\tilde{E}_j}{\partial t^2} = \frac{1}{\varepsilon_0\mathrm{c}^2}\frac{\partial^2\tilde{I}_j}{\partial t^2} \tag{18}$$

where the source term $\tilde{I} = \varepsilon_0\Delta\chi\tilde{E} = \varepsilon_0\rho_0^{-1}\gamma_e\tilde{\rho}\tilde{E}$ indicates the nonlinear polarization.

The coupled wave equations for the interaction of the optical waves and the acoustic wave in the Brillouin-enhanced FWM process can be obtained by combining Eqs. 14 and 18 and making the slowly varying amplitude approximation:

$$\left(\frac{\partial}{\partial z} + \frac{n_x}{\mathrm{c}}\frac{\partial}{\partial t}\right)E_1 = \mathrm{i}g_o\rho E_2 \tag{19a}$$

$$\left(-\frac{\partial}{\partial z}+\frac{n_x}{\mathrm{c}}\frac{\partial}{\partial t}\right)E_2=\mathrm{i}g_o\rho^*E_1 \tag{19b}$$

$$\left(-\frac{\partial}{\partial z}+\frac{n_y}{\mathrm{c}}\frac{\partial}{\partial t}\right)E_3=\mathrm{i}g_o\rho^*E_4e^{i\Delta kz} \tag{19c}$$

$$\left(\frac{\partial}{\partial z}+\frac{n_y}{\mathrm{c}}\frac{\partial}{\partial t}\right)E_4=\mathrm{i}g_o\rho E_3e^{-i\Delta kz} \tag{19d}$$

$$\left(\frac{\partial}{\partial t}+\frac{\Gamma_\mathrm{B}}{2}\right)\rho=\mathrm{i}g_a\left(E_1{E_2}^*+{E_3}^*E_4e^{i\Delta kz}\right) \tag{19e}$$

where the effective refractive indexes of the two polarization axes of the PMF n_x and n_y are related to the optical frequency; g_o and g_a are coupling coefficients of the optical wave and acoustic wave, respectively; and $g_\mathrm{B}=4g_og_a/\Gamma_\mathrm{B}$ is the Brillouin gain factor.

Characteristics of the BDG Reflection Spectrum

Under the steady-state condition with a uniform BDG generated by two continuous pump waves and considering the slowly varying envelope approximation, the analytic expressions of the probe wave E_3 and the reflection wave E_4 can be obtained, and the coupled equations for the latter two optical waves can be simplified as follows:

$$\begin{aligned}\frac{\partial E_3}{\partial z}&=-\mathrm{i}g_o\rho*E_4e^{-i\Delta kz}\\ \frac{\partial E_4}{\partial z}&=\mathrm{i}g_o\rho E_3e^{i\Delta kz}\end{aligned} \tag{20}$$

The analytical expression of the reflection wave E_4 can be expressed as follows:

$$E_3(z)=E_3(L)\cdot\frac{2g\cosh(gz)-i\Delta k\sinh(gz)}{2g\cosh(gL)-i\Delta k\sinh(gL)}e^{-i\Delta k(z-L)/2} \tag{21a}$$

$$E_4(z)=E_3(L)\cdot\frac{2K_2\sinh(gz)}{2g\cosh(gL)-i\Delta k\sinh(gL)}e^{-i\Delta k(z+L)/2} \tag{21b}$$

where $K_1=-\frac{1}{2}g_\mathrm{B}E_1^*E_2$, $K_2=-\frac{1}{2}g_\mathrm{B}E_1E_2^*$ and g is related to $g^2=K_1K_2-(\Delta k)^2/4$.

The reflectivity of the BDG in steady state can be expressed as

$$R=\frac{|E_4(L)|^2}{|E_3(L)|^2}=\frac{\sinh^2(gL)}{\cosh^2(gL)-\Delta k^2/(4K_1K_2)} \tag{22}$$

In most of the BDG experiments, the pump 1 power is much higher than the pump 2 power for a strong BDG distribution. In order to achieve a strong reflected signal from the BDG, the probe power is also chosen to be on the same order as the pump 1 power. Therefore, a more reasonable approximation compared to a moving FBG model is that the pump 1 and probe powers are undepleted, since the length of PMF used in the experiments is short, usually less than tens of meters. Moreover, since the probe power is also high in most experiments, the reflected signal also experiences an SBS amplification. With these assumptions, the numerical and the analytical solutions are compared and analyzed with the simulation parameters shown in Table 1, with the results shown graphically in Fig. 7.

From Fig. 7a, it can be observed that the analytical solutions (the black line for 0.5 m and the blue one for 1 m) agree well with the numerical solutions (the red dots for 0.5 m and the pink ones for 1 m). The full width at half-maximum (FWHM) of

Table 1 The simulation parameters

Parameter	Value
Power of pump 1	0.1 W
Power of pump 2	0.01 W
Power of probe	0.1 W
Fiber length (L)	1.0/0.5 m
Brillouin gain spectrum linewidth	30 MHz
Brillouin gain factor (g_B)	2.5×10^{-11} m/W
Phonon lifetime (τ_p)	5.3 ns
Effective modal area (A_{eff})	50 μm^2
Effective refractive index of slow axis (n_x)	1.4686
Effective refractive index of fast axis (n_y)	1.4683

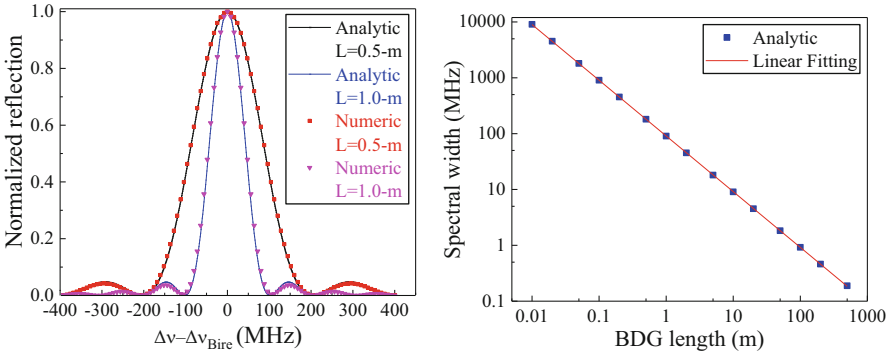

Fig. 7 (**a**) The normalized BDG spectra; (**b**) the spectrum width (FWHM) versus BDG length

the BDG reflection spectrum is inversely proportional to the BDG length, which is shown in Fig. 7b, indicating that the spectral width becomes narrower as the BDG is lengthened.

Distributed Birefringence Measurement of PMFs and Its Sensing Applications

As stated above, the polarization characteristic of a PMF can be described using the phase birefringence and the group birefringence. The former represents the effective refractive index difference of the two polarization axes, which affects the polarization-maintaining capacities; and the latter is connected with the fiber group velocity, which is as a consequence of the fiber dispersion. In Section I, the Sagnac interferometer was introduced as well as its potential use for the measurement of the average group birefringence. For PMFs dominated by stress-induced birefringence with a small dispersion, it is not necessary to distinguish between phase birefringence and group birefringence, and hence the Sagnac interferometer can be used to evaluate the polarization-maintaining properties of the Panda fiber. However, it should be clarified that for the shape-induced PMFs, it is common that phase birefringence and group birefringence differ quite significantly, and thus they need to be measured separately using different measurement methods in order to characterize the PMF.

In this section, the distributed measurement of phase birefringence of a PMF using a BDG is theoretically analyzed and experimentally investigated. The phase birefringence of PMFs is verified by using the two-dimensional finite element numerical calculations and experimental measurements based on BDG. In addition, some sensing applications of birefringence measurement using a BDG are introduced, including simultaneously distributed temperature and strain measurement and distributed measurement of transverse pressure and hydrostatic pressure.

Numerical Calculations of the Birefringence

From Eq. 11, it is clear that the phase birefringence is proportional to the frequency shift between the probe and the co-propagating pump, defined as BireFS, indicating that the BDG can be used to evaluate the phase birefringence. The following content will provide further discussion for the phase birefringence measurement with BDG by comparing the numerical and experimental results.

First, the theoretical values of the phase birefringence and group birefringence are calculated using a two-dimensional finite element analysis method. Four different kinds of commercial PMFs as shown photographically in Fig. 8, including a Panda fiber (PMF-a), an elliptical core (ECORE) fiber (PMF-b), and

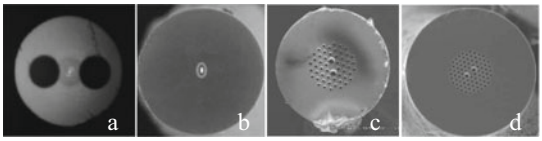

	PMF-a	PMF-b	PMF-c	PMF-d
Type	Panda	ECORE	PCF	PCF
Dia. (μm, cladding)	125	125	99	125
ν_B (GHz, 25℃)	10.871	9.894	11.084	11.063

Fig. 8 The cross sections (upper) and the parameters (lower) of the FUT

Table 2 Calculated phase birefringence and group birefringence of the FUTs

	PMF-a	PMF-b	PMF-c	PMF-d
λ (nm)	1550			
Phase birefringence (10^{-4})	3.748	1.12	3.61	4.86
Group birefringence (10^{-4})	3.806	−2.02	−6.81	−8.71

two polarization-maintaining photonic crystal fibers (PM-PCFs) (PMF-c, PMF-d) are investigated as the fibers under test (FUT).

Among the four PMFs, the birefringence of the Panda fiber is induced by anisotropic stress surrounding the core, which is classified as the stress-induced birefringence PMF, and those of the ECORE fiber and the PM-PCFs, already used in fiber sensing applications for the temperature stability and high-birefringence characteristics, are induced by the imperfect symmetry geometrical effect, which are classified as the shape-induced birefringence PMF.

The phase birefringence is calculated for a set of incident wavelength, and the nonlinear relationship between the phase birefringence and the incident wavelength is numerically approximated with a quartic polynomial. Consequently the dispersion term $d\Delta n/d\lambda$ can be obtained and Δn^g calculated using Eq. 3. The calculated results for the four different PMFs are shown in Fig. 9, which show that the phase birefringence and group birefringence are different. For the shape-induced birefringence PMF, the values of phase birefringence and group birefringence not only differ in magnitude but have opposite signs. For stress-induced birefringence PMF, PMA-a, the absolute values of the phase birefringence and group birefringence exhibit very small difference at the long wavelength range.

The calculated phase birefringence and group birefringence of the four FUTs under the wavelength of 1550 nm are summarized in Table 2

The results show that there are large differences between the phase birefringence and group birefringence for PMF-b, PMF-c, and PMF-d, not only in opposite signs but also the absolute value. One of the major reasons for a large group birefringence is the dispersion, which is caused by the geometric asymmetry in structure, out of concentricity (or airhole distribution for PM-PCFs) and optical modal diffusion.

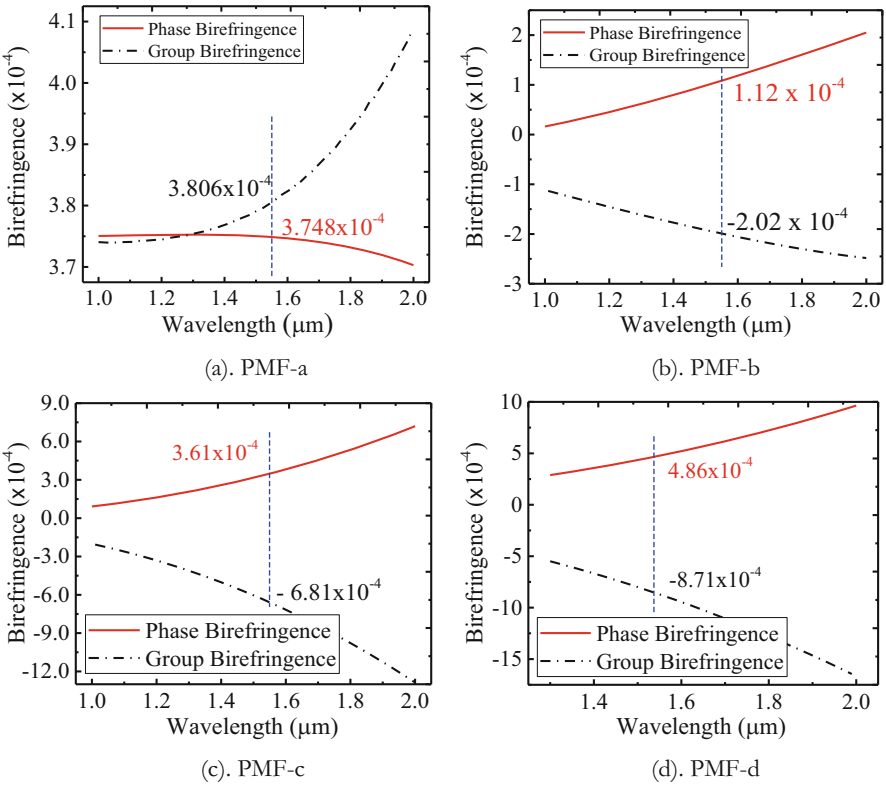

Fig. 9 Simulation results of birefringence for the four types of PMFs

Distributed Phase Birefringence Measurement of the PMFs with BDGs

Experimental Measurement for Different PMFs

Although several effective methods have been proposed for birefringence measurement as referred to in Section I, to date all of them have concentrated on point sensors that can measure only the average birefringence of the test fiber and cannot characterize the birefringence variation along the fiber. As verified earlier in this chapter, under the phase-matching condition expressed by Eq. 12, the phase birefringence can be obtained with the BireFS, which can be obtained through the reflected spectrum of the BDG, and can be measured to evaluate the polarization property with the BDG technique. Using a pulsed probe wave, position-dependent time delays occur for the grating reflection signals at different fiber axial positions, which provide the possibility of distributed phase birefringence measurement. In this section, the distributed phase birefringence measurement of PMF using BDG is discussed, and typical measurement results are provided.

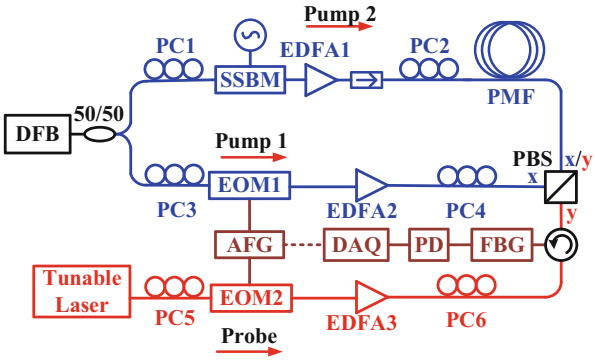

Fig. 10 Experimental setup for generating and probing a BDG

In the birefringence measurement scheme presented, a relatively long pump 1 pulse, a continuous-wave pump 2, and a short probe pulse are chosen to generate and detect the BDG in a PMF, where the long pump 1 pulse can effectively excite a BDG with a relatively low power to avoid other nonlinear effects, i.e., self-phase modulation or modulation instability, thus extending the measurement range in a long-length fiber, and the short probe pulse is used to provide good spatial resolution.

In this case, the configuration presented in Fig. 3a was adopted, and the experimental setup for generating and probing a BDG is shown in Fig. 10. A narrow linewidth distributed feedback (DFB) laser diode with a center wavelength at ~1550 nm and a tunable laser were used as light sources of the pumps and the probe, respectively, with a frequency difference of several tens of GHz according to the BireFS of the FUT. The original frequency wave output from the DFB is regarded as the Brillouin pump wave (pump 1), while the Brillouin Stokes wave (pump 2) is generated by a single-sideband modulator (SSBM) and microwave generator. Two high extinction ratio electrooptic modulators (EOMs) were used to generate the pump 1 and the probe pulses. The two pump waves were polarized to the x polarization state, and the probe wave was polarized to y polarization state through the use of polarization controllers (PCs) and a polarization beam splitter (PBS). The BDG is generated following the pump 1 pulse along the fiber through the SBS process between pulsed pump 1 and continuous pump 2 and detected by the short probe pulse injected immediately following pump 1. The reflected wave is recorded using a photodiode (PD) and photo-amplifier whose output is connected to a data acquisition (DAQ). A reflection spectrum is obtained by sweeping the frequency of the tunable laser.

For this scheme, the spatial resolution of the measurement is determined by the duration of the probe pulse, and hence a high spatial resolution can be obtained using a short probe pulse (Song et al. 2016). The duration of the pump 1 pulse should be larger than that of the acoustic wave (~10 ns) so that the latter can grow to its full extent through the SBS process realizing efficient excitation of the BDG. This setup has proved to be an effective scheme for long-range and high spatial resolution

Table 3 Group birefringence of the FUTs detected by a Sagnac interferometer

	PMF-a	PMF-b	PMF-c	PMF-d
$\Delta\lambda$ (nm)	1.46	1.09	0.612	0.406
Length (m)	4.06	9.83	5.7	7.5
λ (nm)	1550			
Δn_g (10^{-4})	4.05	2.25	6.89	7.89

distributed birefringence measurement without unwanted pump power depletions and nonlinear effects, i.e., self-phase modulation or modulation instability (Dong et al. 2013).

A comparison of the group birefringence as detected by the Sagnac interferometer and calculated according to Eq. 6 is shown in Table 3. The results agree well with the calculated group birefringence shown in Fig. 9 which vindicates the use of the simulation model.

Figure 11 shows the typical measurement results of phase birefringence distributions of the four PMFs using a BDG. The measurement results exhibit good agreement with the corresponding calculated results shown in Fig. 9, which confirms the validity of the phase birefringence measurement using a BDG in both theory and practice.

The data summarized in Table 4 lists the simulation and experiment results of birefringence for the four FUTs. The variance between the simulation and experiment results is quantified using the ratio of phase birefringence to group birefringence (PGR) which has been introduced as a reference parameter. The distributed phase birefringence is obtained in the case of a large value fluctuation. The average phase birefringence value along the FUTs in the case of simulation and experiments was selected to be comparable (as close as possible) in each case (Table 4).

From the comparison of the results and analysis above, the BDG clearly measures the phase birefringence, and for most PMFs, the phase and group birefringence values are different, especially for the shape-induced PMF such as PM-PCFs which have relatively large dispersion value. Thus, for evaluation of the polarization characteristics of certain kinds of PMFs, the selection of the birefringence detection methods should be carefully considered: the Sagnac method is a suitable group birefringence measurement method, while the BDG can be an effective method for distributed phase birefringence measurement.

Extension of the Measurement Range

It has already been stated that the BDG can be generated using two counter-propagating pump waves through the SBS interaction, and when the BDG is generated in the slow axis of a PMF, there are two possible probing processes which are defined according to the relative movement directions of the probe wave and the BDG. One is the coherent Stokes Brillouin scattering with the two propagating in the same direction, where the reflected wave frequency is down-converted by a fiber

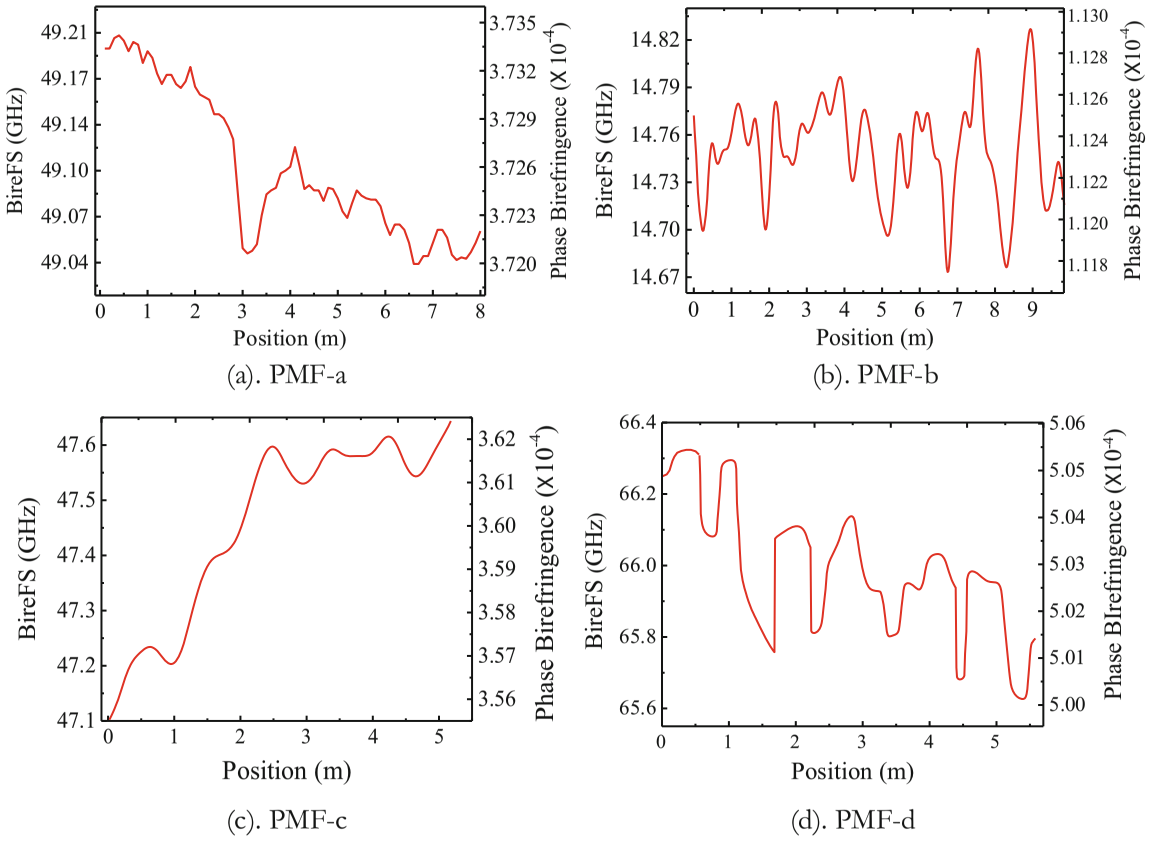

Fig. 11 Typical examples of measured phase birefringence distributions of the four PMFs

Table 4 Birefringence of different PMF samples ($\lambda = 1550$ nm)

	Simulation results			Experiment results		
	Phase (10^{-4})	Group (10^{-4})	PGR	BDG phase (10^{-4})	Sagnac group (10^{-4})	PGR
PMF-a	3.748	3.806	0.98	3.73	4.05	0.92
PMF-b	1.12	−2.02	−0.55	1.12	2.25	0.50
PMF-c	3.61	−6.81	−0.53	3.60	6.89	0.52
PMF-d	4.866	−8.71	−0.56	5.02	7.89	0.64

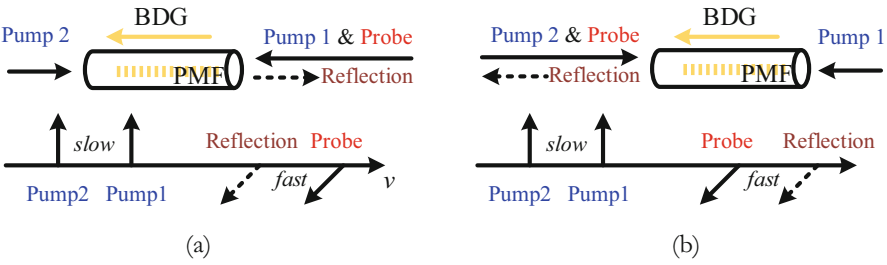

Fig. 12 BDG probing schemes of (**a**) coherent Stokes Brillouin scattering and (**b**) coherent anti-Stokes Brillouin scattering

BFS as shown in Fig. 12a; the other is the coherent anti-Stokes Brillouin scattering process for which the probe wave and the BDG propagating in opposite directions, resulting in a frequency up-converted reflected wave, as shown in Fig. 12b (Dong et al. 2010b). If two continuous-wave (C.W.) light sources are used to excite the BDG, a serious pump depletion occurs that greatly limits the measurement range.

In the investigation of this article, a scheme using a pulsed pump and a continuous pump is adopted in order to extend the measurement distance. Through optimizing the pumping and probing scheme, long-range and high spatial resolution distributed birefringence measurement can be achieved. There are two schemes of BDG generation according to the energy transfer direction between the two pumps: the pump pulse attenuated scheme and the pump pulse amplified scheme depending on whether the energy is transferred to or from the pulsed pump (Dong et al. 2013).

Pump Pulse Attenuated Scheme

In order to minimize the depletion effect between the two pumps, the pump pulse attenuated scheme shown in Fig. 13 was adopted, involving a C.W. pump 2, a relative long pump 1 pulse, where the latter can effectively excite a BDG with a relatively low power to avoid additional nonlinear effects in a long fiber, and the short probe pulse was used to improve the spatial resolution. The frequency of pump 1 is higher than that of pump 2 with a BFS, such that the energy of pulsed pump 1 is transferred to C.W. pump 2. The energy of pump 1 is therefore attenuated following

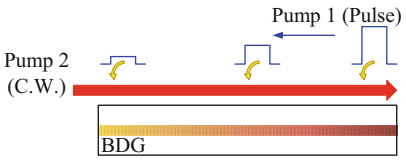

Fig. 13 The schematic diagram of the pump pulse attenuated BDG

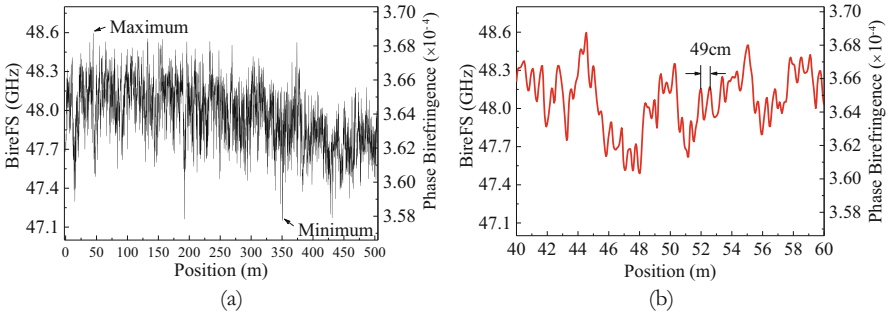

Fig. 14 The measured birefringence over (**a**) the entire 500 m FUT and (**b**) the segment of 40–60 m

a long transmission through the fiber. The duration of pulsed pump 1 limits the interaction length between the two pumps, so as to minimize the depletion of the higher-frequency pump 1 power.

Figure 14a shows the distributed phase birefringence measurement results of a 500 m length of Panda fiber with a 20 cm spatial resolution (Dong et al. 2013) using the pump pulse attenuated BDG shown in Fig. 13. The maximum phase birefringence achieved was 3.6869×10^{-4} located at the position of 44.55 m, and the minimum value was 3.5772×10^{-4} located at the position of 350.65 m, resulting in a fluctuation of ~3% over the entire length of the fiber. The detailed birefringence distribution for the fiber segment of 40–60 m is shown in Fig. 14b. The results show a periodic variation of the birefringence with a spatial period of 49 cm, which corresponds to the spatial period of the fiber spool. It indicates that the fiber is subject to uneven stress when wound to the spool, and the birefringence variation could result from both uneven axial stress and uneven transverse pressure between different fiber layers, and it can be observed that the change of BireFS caused by the uneven stress is in the range of a few hundreds of megahertz (the difference between maximum and minimum BireFS values in the trace).

In addition to the peaks with a spatial period of 49 cm, there exist several other peaks with longer spatial periods, which could be caused by the residual stress induced by various disturbance factors, e.g., during the fiber drawing and coating processes or the nonuniformity in the fiber preform.

Pump Pulse Amplified Scheme

For the pump pulse attenuated scheme, although the interaction length between the two pumps is limited and the pump depletion is minimized, the continuous power

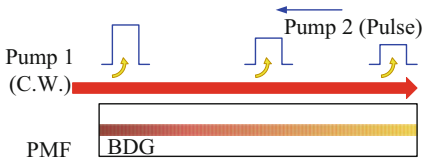

Fig. 15 The schematic diagram of the pump pulse amplified BDG.

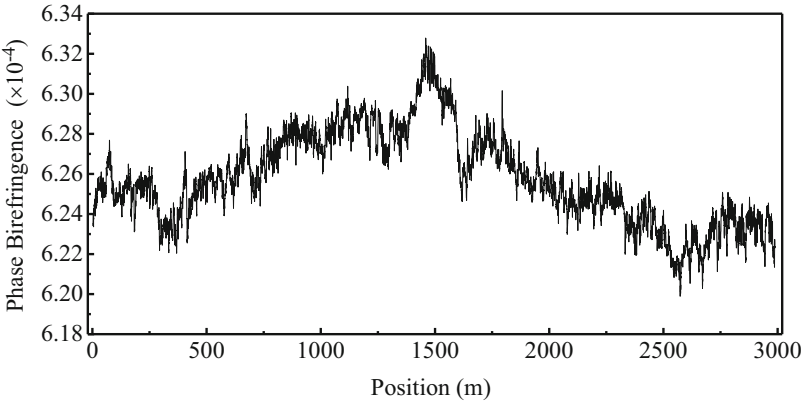

Fig. 16 The measured birefringence over the entire 3 km FUT

attenuation of the pulsed pump will still weaken the signal intensity, which limits the measurement range.

The pump pulse amplified BDG with a C.W. pump 1 and a pulsed pump 2 is shown in Fig. 15, where the frequency of the former is higher than that of the latter by a BFS. Because of the time invariance C.W. pump 1, the energy transferred from pump 1 to pump 2 remains constant, and the latter is continuously amplified, enabling stable BDG excitation at all axial positions along the entire fiber.

Figure 16 shows the distributed phase birefringence measurement results of a 3 km Panda fiber with a 20 cm spatial resolution using the pump pulse amplified BDG. It is worth noting that the distribution symmetry of the phase birefringence is caused by winding, and the periodic variation of birefringence is caused by the nonuniform distribution of stress or transverse pressure when winding the fiber onto the spool. Such a nonuniform stress distribution measurement is of great use in the field of online monitoring of fiber fabrication and fiber gyro evaluation.

Sensing Applications

In recent years, distributed optical fiber sensors based on Brillouin scattering have gained much interests owing to their inherent advantages of long-range measurement, high spatial resolution, and high accuracy. However, the existing Brillouin-based distributed fiber sensors, such as Brillouin optical time-domain

analysis (BOTDA) and Brillouin optical correlation-domain analysis (BOCDA), are limited by a narrow measurement range, only being able to measure distributed temperature and strain (Martynkien et al. 2010; Bao and Chen 2011), which has restricted the growth of such distributed fiber sensors. In this section, the sensing applications of the BDG birefringence measurement are discussed. The sensing mechanism of a BDG derives from the sensitivity of the fiber birefringence to externally applied environmental parameters. The strain, temperature, and pressure fields affect the response of the fiber birefringence directly through expansion and compression of the fiber size and through the electrooptical effect, which results in the external perturbation-induced modification of the birefringence. On the basis of distributed birefringence measurement, a wider range of sensing applications can be realized, which provide numerous new and excellent opportunities for distributed fiber sensing.

Distributed Temperature and Strain Measurement

The existing Brillouin scattering-based distributed fiber sensor can realize distributed temperature and strain measurement, separately, through measuring the BFS distribution. However, since both strain and temperature can produce a BFS change, these distributed sensors are inevitably subject to cross sensitivity to these parameters. This is a regularly encountered problem when attempting discrimination of temperature and strain. Formerly, an additional measurable parameter, which has an independent relationship with strain and temperature, has been induced to allow separation of temperature and strain measurement. The BireFS associated with a BDG can be employed as the supplementary parameter to realize simultaneous and independent temperature and strain measurement.

It has been proved that phase birefringence can be introduced as the second parameter to simultaneously and completely discriminate the strain and temperature using a single length of Panda PMF (Zou et al. 2009). Two independent parameters in a fiber, the BFS and phase birefringence, were measured to obtain two independent responses to strain and temperature. Compared with the positive strain and temperature coefficients of BFS, the phase birefringence has a positive strain coefficient and negative temperature coefficient, which ensures a high discrimination accuracy.

The BireFS and BFS distributions obtained by the BDG and typical BOTDA can be used to determine the temperature and strain, which were described given by Dong et al. (2010c) as follows:

$$\begin{bmatrix} \Delta\varepsilon \\ \Delta T \end{bmatrix} = \frac{1}{C_{\mathrm{B}}^{\varepsilon} C_{\mathrm{Bire}}^{T} - C_{\mathrm{B}}^{T} C_{\mathrm{Bire}}^{\varepsilon}} \begin{bmatrix} C_{\mathrm{Bire}}^{T} & -C_{\mathrm{B}}^{T} \\ -C_{\mathrm{Bire}}^{\varepsilon} & C_{\mathrm{B}}^{\varepsilon} \end{bmatrix} \begin{bmatrix} \Delta v_{\mathrm{B}} \\ \Delta v_{\mathrm{Bire}} \end{bmatrix} \tag{23}$$

where ΔT and $\Delta\varepsilon$ are changes in strain and temperature, respectively, and $C_{\mathrm{B}}^{\varepsilon}$, C_{B}^{T}, $C_{\mathrm{Bire}}^{\varepsilon}$, and C_{Bire}^{T} are coefficients of strain and temperature related to BFS and BireFS, respectively. Here, $C_{\mathrm{B}}^{\varepsilon}$, C_{B}^{T}, and $C_{\mathrm{Bire}}^{\varepsilon}$ have a positive sign, while C_{Bire}^{T} has

a negative sign, and hence $C_{\mathrm{B}}^{\varepsilon}C_{\mathrm{Bire}}^{T} - C_{\mathrm{B}}^{T}C_{\mathrm{Bire}}^{\varepsilon}$ is a large value, which ensures a high discrimination accuracy (Zou et al. 2009).

The individual temperature and strain dependences of BFS of the Panda fiber were measured using a standard BOTDA system, with $C_{\mathrm{B}}^{T} = 1.12$ MHz/°C and $C_{\mathrm{B}}^{\varepsilon} = 0.0482$ MHz/$\mu\varepsilon$, respectively. The dependence of the BireFS on temperature and strain were measured, and temperature and strain coefficients of BireFS were $C_{\mathrm{Bire}}^{T} = -54.38$ MHz/°C and $C_{\mathrm{Bire}}^{\varepsilon} = 1.13$ MHz/$\mu\varepsilon$ as shown in Fig. 17, which indicates that the BireFS provides a higher sensitivity for temperature and strain measurement compared with the BFS.

A 6 m Panda fiber is used to conduct the temperature and strain simultaneous measurement experiment, with a 1 m segment stressed under a strain of 670 $\mu\varepsilon$ and 1 m segment heated under the temperature higher than room temperature by 30 °C, as shown in Fig. 18.

The BFS was obtained using a one-peak Lorentz fitting, and the BFS difference (subtracting the BFS at room temperature and loose state) is shown in Fig. 19a. The BireFS difference (subtracting the BireFS at room temperature and loose state) is also shown in Fig. 19a. The measured strain and temperature coefficients and distributions of BireFS and BFS along the sensing fiber are shown in Fig. 19a, and these in turn allow the distributions of the strain and temperature to be simultaneously calculated as shown in Fig. 19b. The fitting uncertainty of BFS is 0.4 MHz, corresponding to the temperature and strain accuracy of the discrimination of $\delta T = 0.36$ °C and $\delta\varepsilon = 8.3$ $\mu\varepsilon$, and the fitting uncertainty of BireFS is 3 MHz, corresponding to $\delta T = 0.06$ °C and $\delta\varepsilon = 2.7$ $\mu\varepsilon$. Therefore the BireFS provides higher accuracy compared to BFS, as the discrimination accuracy is limited by the

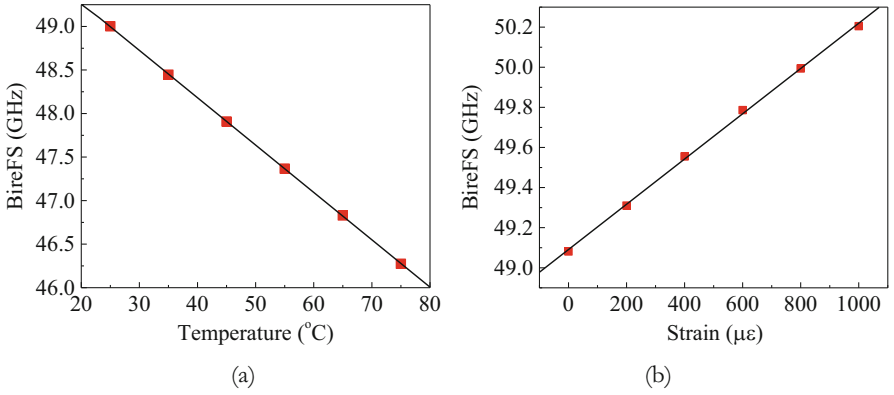

Fig. 17 The dependence of BireFS on (**a**) temperature and (**b**) strain of the Panda fiber

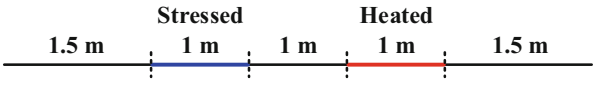

Fig. 18 Layout of the 6 m sensing fiber with a 1 m stressed segment and 1 m heated segment

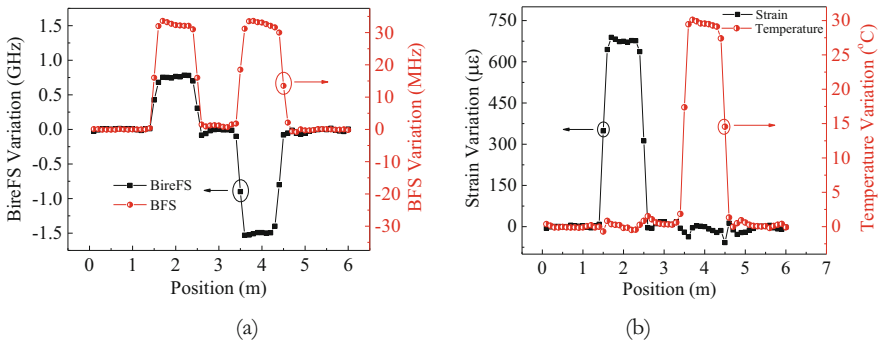

Fig. 19 (**a**) Measured BireFS and BFS and (**b**) calculated temperature and strain

uncertainty of BFS. From the results in Fig. 19, it can be seen that the temperature and strain can be discriminated from each other except at the transition regions, at which the uncertainty in BFS and BireFS due to the spatial resolution causes the error.

Distributed Transverse Pressure Measurement

In recent years, transverse pressure sensing techniques have gained much attention mainly due to the increasing demands on high-sensitivity non-axisymmetric pressure detection in fields of structural health monitoring and civil engineering (Kringlebotn et al. 1996; Shao et al. 2010). The reliable and effective measurement of transverse pressure is needed in actual manufacture. The traditional fiber transverse pressure sensor has largely been based on a FBG with a high-sensitivity and a simple structure (Jewart et al. 2006; Zu et al. 2011); however, it cannot realize distributed measurement. Although Brillouin scattering-based fiber sensors have existed for two decades and are widely used in external physical parameter distributed sensing areas, such as temperature and strain, the traditional Brillouin distributed fiber sensing systems are insensitive to transverse pressure.

Fiber birefringence changes because of the elastic-optical effect when subjected to the transverse pressure. Distributed transverse pressure measurement can be realized by measuring the birefringence changes using a BDG. Figure 20 shows the self-designed pressure applying platform with a 10-m-long test fiber and a support fiber embedded between a 20 cm glass plate and a controllable metal support platform. An ECORE fiber is used as FUT due to its lower sensitivity to temperature. The temperature sensitivity of ECORE fiber is almost an order of magnitude lower than that of Panda fiber, hence resulting in weaker temperature cross talk. A SMF is used as the supporting fiber; since the SMF has the same structural mechanical properties as the test fiber, including the geometric size, the Young's modulus, and the Poisson's ratio, when applying the pressure in the middle of the two fibers, each fiber carries half of the pressure. The sensing fiber is maintained with a low axial strain to prevent unwanted twist by the two rotary mounts. By rotating the mounts,

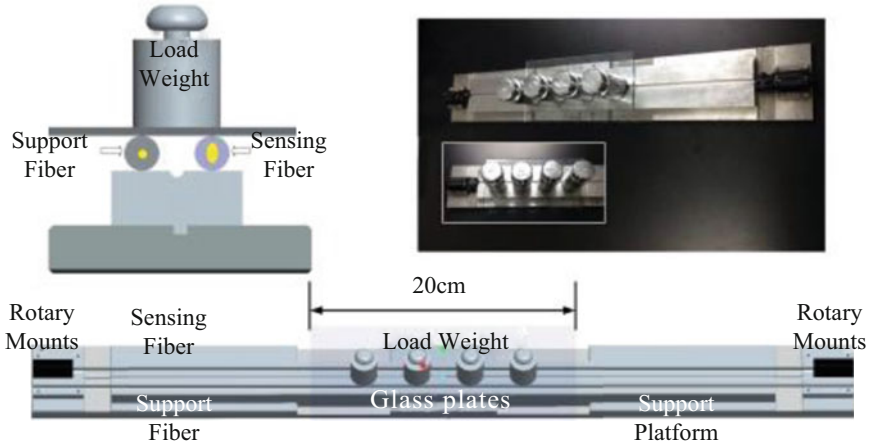

Fig. 20 Setup of pressure weight applied with two rotary mounts

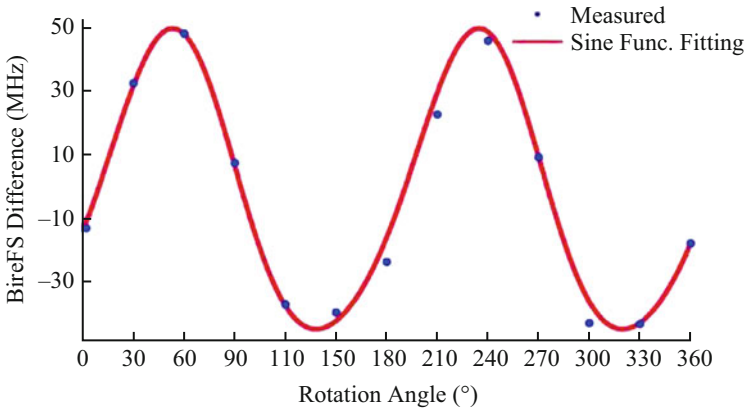

Fig. 21 Change in birefringence as a function of pressure direction

the angle between the direction of application of the pressure and the fiber axis can be adjusted (Dong et al. 2015).

Figure 21 indicates the birefringence change as a function of the pressure direction. The measured results (blue dots) agree well with a sinusoidal fitting curve, where the maximum increment of birefringence appears at the slow-axis direction (50° and 230°) while the maximum decrement at the fast-axis direction (140° and 320°)

Figure 22 shows the transverse pressure dependences of BireFS of the ECORE fiber and Panda fiber. The results for ECORE fiber in Fig. 22a illustrate the transverse pressure sensitivities of 6.217 GHz/Nmm^{-1} for the fast-axis direction and 6.28 GHz/Nmm^{-1} for the slow-axis direction. And for the Panda fiber shown in

Fig. 22b, the measured sensitivities are 4.097 GHz/Nmm^{-1} and 3.439 GHz/Nmm^{-1} for the slow and fast axes, respectively (Dong et al. 2015).

To verify the distributed measurement and the direction-sensitive abilities of transverse pressure sensing, the simultaneous measurement of two transverse pressures applied on two separate fiber locations is performed, with one pressure along the fast axis and the other along the slow. The results are shown in Fig. 23, where the red and green lines represent the measured BireFS distributions with and without pressure, respectively, and the blue line represents the BireFS difference and the corresponding transverse pressure. The position, magnitude, and direction of the pressure can be distinguished in Fig. 23.

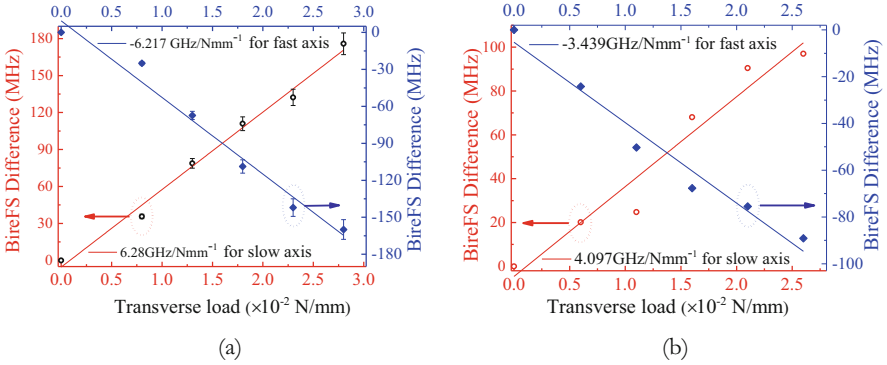

Fig. 22 BireFS differences versus transverse pressures for (**a**) ECORE fiber and (**b**) Panda fiber

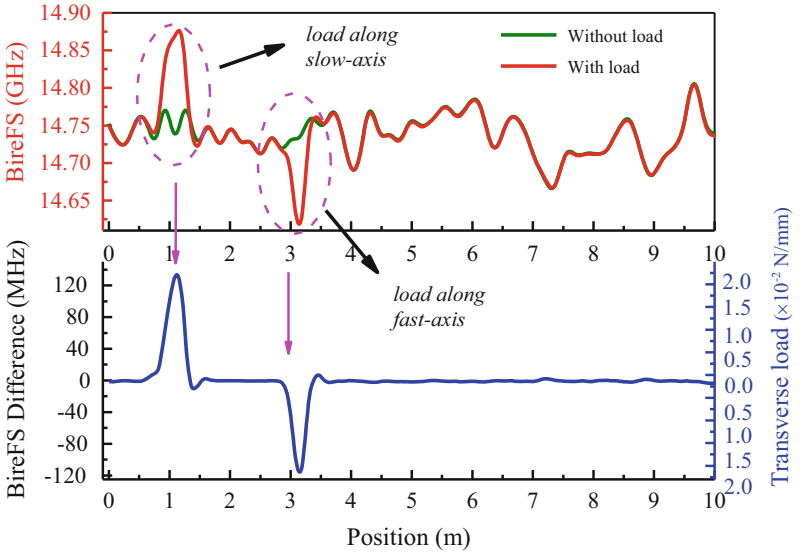

Fig. 23 Results of the distributed transverse pressure measurements

Distributed Hydrostatic Pressure Measurement

Hydrostatic pressure measurement is widely needed for a variety of areas, such as automotive production, aerospace engineering, and harsh environment detection. Currently available optical fiber hydrostatic pressure sensors are mainly based on the FBGs and interferometric sensors (Tarnowski et al. 2013; Bhowmik et al. 2015) which are point sensors that cannot realize distributed measurement. Distributed hydrostatic pressure sensing is needed in several industrial application areas, e.g., for measurement of oil well pressure with high temperature and where the pressure range is ultrahigh, being above 100 MPa. It would be highly significant for the oil-gas production to be able to successfully realize distributed hydrostatic pressure measurement.

When the fiber experiences the hydrostatic pressure, its birefringence will change because of the elastic-optical effect, based on which, hydrostatic pressure along the fiber can be measured by detecting the birefringence change of the fiber using a BDG.

A PM-PCF is adopted as the test fiber to conduct the distributed hydrostatic pressure measurement experiment. This kind of fiber features a porous structure, a facility to deform, and a pure silica material. The thermal expansion coefficients between the solid core and the porous cladding of the pure silica PM-PCF are approximately equal; therefore, there is a lower-temperature birefringence coefficient, and the temperature cross talk can be more accurately compensated. These characteristics make it a highly suitable choice for increasing the measurement sensitivity and decreasing the temperature cross talk effect (Teng et al. 2016).

Figure 24 shows the layout of the PM-PCF which is divided into three parts with two 20 cm pressurized parts in a self-designed pressure vessel and a heated part in a controllable oven, where the inset shows the cross section of the PM-PCF.

The temperature and hydrostatic pressure dependences of BFS of the PM-PCF are investigated using the typical BOTDA system, with the results shown in Fig. 25, which indicates the temperature dependence of the BFS, with a coefficient of 1.07 MHz/°C. And it can be seen that the BFS has low sensitivity to hydrostatic pressure, with a maximum BFS fluctuation of only 1.88 MHz within the pressure range of 0–1.1 MPa, which can be neglected.

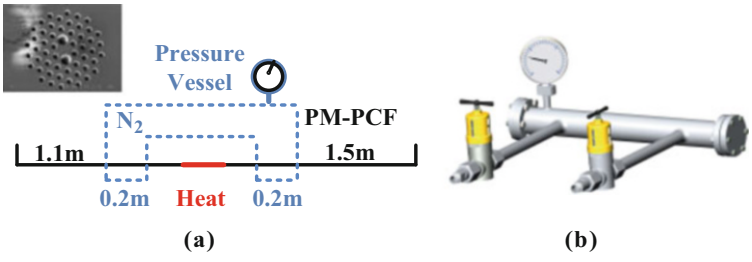

Fig. 24 (**a**) The cross section and layout of the FUT and (**b**) the self-designed pressure vessel

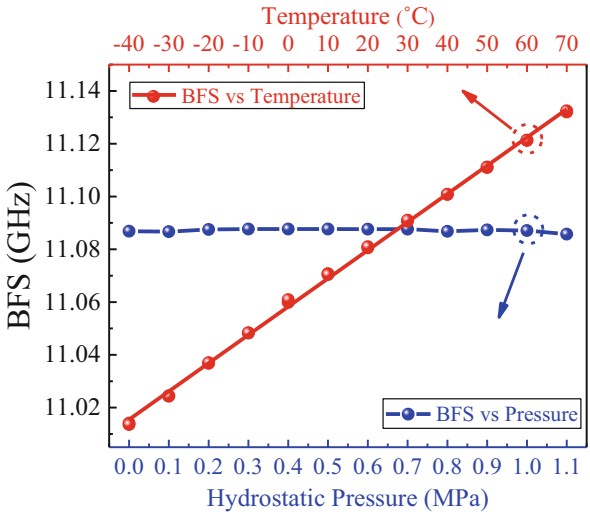

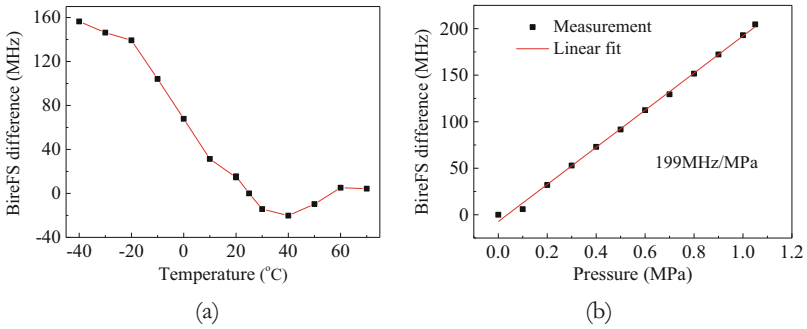

Fig. 25 The temperature and hydrostatic pressure dependences of BFS of the PM-PCF

Fig. 26 Measured BireFS differences of PM-PCF versus the (**a**) temperature and (**b**) hydrostatic pressure

In order to eliminate temperature cross talk effects on the birefringence changes, the first step is to interrogate BFS changes by obtaining the temperature distribution over the FUT and then obtain the BireFS changes of the FUT induced when both temperature and pressures are interrogated. Next, the effect on the fiber birefringence from the ambient temperature can be subtracted according to the measured temperature distribution. Consequently, the hydrostatic pressure-induced birefringence changes without temperature disturbance can be isolated.

The temperature and hydrostatic pressure dependences of the BireFS of the PM-PCF have been investigated with the results shown in Fig. 26.

Figure 26a shows the measured BireFS with respect to temperature, with a maximum difference of 176 MHz for the temperature range of −40 °C to 40 °C. The characteristic of the nonlinear temperature dependence of birefringence is mainly due to the effect of coating material. The standard deviation of temperature measurement of BOTDA is about ±0.5 °C, which corresponds to temperature-induced

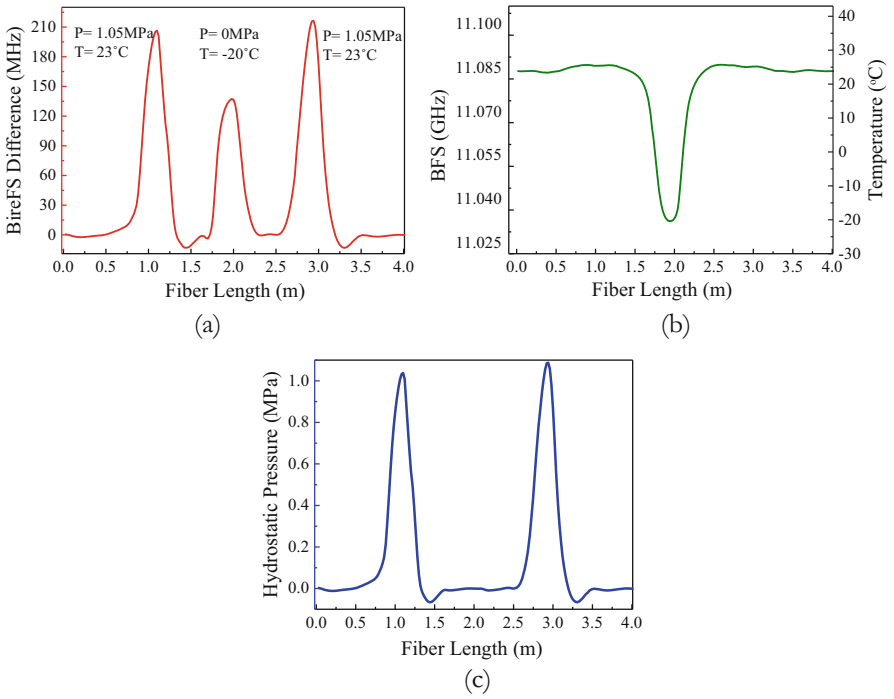

Fig. 27 Results of temperature-compensated distributed hydrostatic pressure sensing, (**a**) the measured BireFS difference of the FUT, (**b**) the measured BFS of the FUT, and (**c**) the measured hydrostatic pressure with temperature compensation

BireFS changes of ±1.1 MHz for the PM-PCF and BireFS changes of ±27.5 MHz for Panda. From Fig. 26, it can be calculated that the BireFS changes at ±1.1 MHz are equivalent to a hydrostatic pressure change of 0.005 MPa; by contrast, the BireFS changes at ±27.5 MHz are equal to a hydrostatic pressure change of ±0.14 MPa. Therefore, the PM-PCF is preferred when compensating for the temperature changes and reducing the cross talk to pressure measurement.

Figure 26b shows the linear dependence of BireFS difference on hydrostatic pressure, with a sensitivity of 199 MHz/MPa. When considering the measurement standard deviation of $\delta\ \nu_{\mathrm{Bire}} = \pm 5$ MHz from the measured distributed BireFS results, the accuracy is as high as 0.025 MPa. When taking the error propagation from the temperature measurement error of 0.5 °C of BOTDA into consideration, the maximum measurement accuracy should be modified to less than 0.03 MPa.

The BFS difference, $\Delta\nu_{\mathrm{B}}$, and BireFS difference, $\Delta\nu_{\mathrm{Bire}}$, caused by temperature and pressure can be expressed as

$$\begin{aligned} \Delta\nu_{\mathrm{B}} &= C_{\mathrm{B}}^{T}\Delta T + \Delta\nu_{\mathrm{B}}^{P} \\ \Delta\nu_{\mathrm{Bire}} &= \Delta\nu_{\mathrm{Bire}}^{T} + C_{\mathrm{Bire}}^{P}\Delta P \end{aligned} \tag{24}$$

where C_{B}^{T} and C_{Bire}^{P} are coefficients to the temperature related to BFS and to hydrostatic pressure related to BireFS, respectively. It has been demonstrated that the pressure-induced BFS changes, $\Delta v_{\mathrm{B}}^{P}$, can be ignored. And the temperature-induced BFS changes, $C_{\mathrm{B}}^{T}\Delta T$, can be obtained from the BOTDA data, and the temperature changes ΔT can be computed. Therefore, the temperature-induced BireFS difference, $\Delta v_{\mathrm{Bire}}^{T}$, can be calculated according to Fig. 26a. Finally, $\Delta v_{\mathrm{Bire}}^{T}$ can be subtracted, and the hydrostatic pressure-induced birefringence changes, $C_{\mathrm{Bire}}^{P}\Delta P$, and the hydrostatic pressure changes ΔP without temperature disturbance can be obtained.

Figure 27 shows the process of extraction of the hydrostatic pressure distributed measurement and the temperature compensation. In Fig. 27a, the hydrostatic pressure (1.05 MPa) and temperature (−20 °C) are simultaneously measured using the BDG. Figure 27b shows the temperature measurement result using a standard BOTDA, which clearly distinguishes the temperature. The hydrostatic pressure measured after temperature compensation is shown in Fig. 27c. The results shown in Fig. 27 are consistent with the results in Fig. 26.

Conclusion

Phase birefringence is an important optical parameter for defining the polarization property of a PMF. Distributed phase birefringence measurement can be realized using the BDG technique, creating a new view of PMF and fiber gyro quality test. In this chapter, the basic principles of distributed birefringence measurement of PMF based on BDG have been introduced. The BDG is an acoustic-modulated weak optical grating obeying the fundamental laws of the standard FBG. The generation and probing of a BDG involve four optical waves, and the FWM model clearly demonstrates this coupling process. The BireFS has a proportional relationship with the phase birefringence, which provides the foundation of birefringence measurement with BDG. The theoretical analysis and numerical simulation of birefringence measurement with BDG have been demonstrated. The chapter is concluded with examples of real sensing applications of distributed phase birefringence measurement with BDG: simultaneous temperature and strain measurement, distributed transverse pressure sensing, and hydrostatic pressure sensing.

References

P. G. Agrawal (ed.), *Nonlinear Fiber Optics* (Academic Press, San Diego, 2007)
X. Bao, L. Chen, Sensors **11**, 4 (2011)
K. Bhowmik, G.D. Peng, Y. Luo, J. Lightwave Technol. **33**, 12 (2015)
S. Chin, L. Thévenaz, Laser Photonics Rev. **6**, 724 (2012)
Y. Dong, X. Bao, L. Chen, Opt. Lett. **34**, 17 (2009)
Y. Dong, L. Chen, X. Bao, Opt. Lett. **35**, 2 (2010a)
Y. Dong, L. Chen, X. Bao, Opt. Express **18**, 18 (2010b)
Y. Dong, L. Chen, X. Bao, IEEE Photon. Technol. Lett. **22**, 18 (2010c)

Y. Dong, H. Zhang, Z. Lu, J. Lightwave Technol. **31**, 16 (2013)
Y. Dong, T. Jiang, L. Teng, Opt. Lett. **39**, 10 (2014)
Y. Dong, L. Teng, P. Tong, Opt. Lett. **40**, 21 (2015)
T. Erdogan, J. Lightwave Technol. **15**, 8 (1997)
H. Eugene (ed.), *Optics* (Pearson Education, San Francisco/Boston/New York, 2002)
X. Fang, R.O. Claus, Opt. Lett. **20**, 20 (1995)
P. Hlubina, D. Ciprian, Opt. Express **15**, 25 (2007)
S. Huang, Z. Lin, Appl. Opt. **24**, 15 (1985)
C. Jewart, K.P. Chen, B. McMillen, Opt. Lett. **31**, 15 (2006)
C. Kaczmarek, Opt. Appl. **42**, 4 (2012)
I. Kaminow, IEEE J. Quantum Electron. **17**, 1 (1981)
G. Keiser (ed.), *Optical fibers communications* (Wiley, New York, 2003)
K. Kikuchi, T. Okoshi, Opt. Lett. **8**, 2 (1983)
D.H. Kim, J.U. Kang, Opt. Express **12**, 19 (2004)
J.T. Kringlebotn, W.H. Loh, R.I. Laming, Opt. Lett. **21**, 22 (1996)
H.C. Lefevre, *The fiber-optic gyroscope* (Artech House, Boston/London, 2014)
S. Li, M.J. Li, Opt. Lett. **37**, 22 (2012)
T. Martynkien, G. Statkiewicz-Barabach, J. Olszewski, Opt. Express **18**, 14 (2010)
J. Noda, K. Okamoto, Y. Sasaki, J. Lightwave Technol. **4**, 8 (1986)
R. Pant, E. Li, C.G. Poulton, Opt. Lett. **38**, 3 (2013)
J. Sancho, N. Primerov, S. Chin, Opt. Express **20**, 6 (2012)
M. Santagiustina, S. Chin, N. Primerov, L. Ursini, L. Thévenaz, Sci. Rep. **3**, 1594 (2013)
L.Y. Shao, Q. Jiang, J. Albert, Appl. Opt. **49**, 36 (2010)
V. Sikka, S. Balasubramanian, A. Viswanath, Appl. Opt. **37**, 2 (1998)
K.Y. Song, Opt. Lett. **36**, 23 (2011)
K.Y. Song, Opt. Express **20**, 25 (2012)
K.Y. Song, J.H. Yoon, Opt. Lett. **35**, 17 (2010)
K.Y. Song, W. Zou, Z. He, Opt. Lett. **33**, 9 (2008)
K.Y. Song, K. Hotate, W. Zou, J. Lightwave Technol. **35**, 16 (2016)
K. Suzuki, H. Kubota, S. Kawanishi, Opt. Express **9**, 13 (2001)
M. Szczurowski, W. Urbanczyk, M. Napiorkowski, Appl. Opt. **50**, 17 (2011)
K. Takada, J. Noda, R. Ulrich, Appl. Opt. **24**, 24 (1985)
K. Tarnowski, A. Anuszkiewicz, J. Olszewski, Opt. Lett. **38**, 24 (2013)
L. Teng, H. Zhang, Y. Dong, Opt. Lett. **41**, 18 (2016)
P.K.A. Wai, C.R. Menyak, J. Lightwave Technol. **14**, 2 (1996)
H.G. Winful, Opt. Express **21**, 8 (2013)
B. Xu, C.L. Zhao, F. Yang, Opt. Lett. **41**, 7 (2016)
W. Zhou, Z. He, K. Hotate, Opt. Express **17**, 3 (2009)
D.P. Zhou, Y. Dong, L. Chen, Opt. Express **19**, 21 (2011)
W. Zou, J. Chen, Opt. Express **21**, 12 (2013)
W. Zou, Z. He, K.Y. Song, Opt. Lett. **34**, 7 (2009)
P. Zu, C.C. Chan, Y. Jin, Meas. Sci. Technol. **22**, 2 (2011)